Available online at www.sciencedirect.com

ScienceDirect

Procedia Structural Integrity 21 (2019) 61–72

Structural Integrity Procedia

www.elsevier.com/locate/procedia

1st International Workshop on Plasticity, Damage and Fracture of Engineering Materials

A Micromechanics Based Numerical Investigation of Dual Phase Steels

Tuncay Yalçinkaya[a,*], Gönül Öykü Güngör[a], Serhat Onur Çakmak[a], Cihan Tekoğlu[b]

[a] Middle East Technical University, Department of Aerospace Engineering, Ankara 06800, Turkey
[b] Department of Mechanical Engineering, TOBB University of Economics and Technology, Söğütözü, Ankara 06560, Turkey

Abstract

The aim of this paper is to investigate the effects of microstructural parameters such as the volume fraction, morphology and spatial distribution of the martensite phase and the grain size of the ferrite phase on the plasticity and localized deformation of dual-phase (DP) steels. For this purpose, Voronoi based representative volume elements (RVEs) are subjected to proportional loading with constant stress triaxility. Two alternative approaches are employed in a comparative way to model the plastic response of the ferrite phase, namely, micromechanically motivated crystal plasticity and phenomenological J2 flow theory. The plastic response of the martensite phase, however, is modeled by the J2 flow theory in all the calculations. The predictions of both approaches closely agree with each other in terms of the overall macroscopic response of the DP steels, while clear differences are observed in the localized deformation patterns. The results of the present study are also compared with experimental and computational findings from the literature.

Keywords: Dual-phase Steel; Representative Volume Element; Crystal Plasticity; Triaxiality; Localization

1. Introduction

DP steels belong to a group of advanced high strength steels which are mainly developed for the needs of automotive industry in 1970's, when low carbon, low alloy steels were in demand. Low alloy content of dual-phase steels have provided high elongation and strength with improved formability along with fatigue and crash resistance with an extra advantage of being light and affordable (see e.g. Tasan et al. (2015) for an overview on the subject). DP steels are composed of brittle martensite islands distributed in a ductile ferrite matrix. The macroscopic mechanical properties ofDP steels are strongly related to their complex microstructure, which on the other hand comes with interesting localization and failure mechanisms at the microscopic scale. Mechanical response of dual-phase steels can be accurately

* Corresponding author. Tel.: +90-312-210-4258 ; fax: +90-312-210-4250.
E-mail address: yalcinka@metu.edu.tr

2452-3216
10.1016/j.prostr.2019.12.087

represented only if both the ferrite and martensite phases are modeled realistically. An accurate model should take into account microstructural features of DP steels such as the volume fraction, morphology, carbon content and spatial distribution of the martensite, and the grain size of ferrite (see e.g. Bag et al. (1999); Kang et al. (2007); Avramovic-Cingara et al. (2009); Kadkhodapour et al. (2011c)). Therefore, micromechanical modeling of dual-phase steels is crucial to understand and capture their bulk and local constitutive response. In this context, the crystal plasticity finite element approach is a good candidate to take into account various effects at the grain scale. There have been several studies addressing these materials through both experiments and crystal plasticity modelling using representative volume elements (see e.g. Kim et al. (2012); Choi et al. (2013); Al-Rub et al. (2015); Jafari et al. (2016); Bong et al. (2017)). In general, the modelling and comparison with experiments have been conducted at regions where uniaxial loading conditions are assumed to occur, yet the effect of stress triaxality has not been discussed before.

In the present study, four different representative volume elements (RVEs) are generated with different martensite volume fractions and spatial distributions to simulate the overall macroscopic as well as the microscopic behavior of DP steels under constant stress triaxiality loading conditions. The focus of the study has been directed on the similarities and differences between the two modelling approaches, i.e. crystal and phenomenological plasticity models.

2. Micromechanical model

2.1. Representative volume element generation

All the RVEs used in this study are three-dimensional (3D) and they are produced by polycrystal generation and meshing software Neper; see Quey et al. (2011). Before proceeding with the simulations for the DP steels, crystal plasticity parameters for the ferrite phase are identified by comparing the overall mechanical response of a 200-grain RVE (containing only randomly oriented ferrite grains) with the experimental tensile data presented in Lai et al. (2016). Once the crystal plasticity parameters are identified, four (approximately) 400-grain RVEs are generated, referred to as DP1, DP2, DP3 and DP4 in the following, each representing a different DP steel with different microstructural features (see Fig. 1, where the green and white zones respectively correspond to the ferritic and martensitic phases). The microstructural features for these four RVEs are given in Table 1. All the finite element (FE) calculations in this study are performed by using the commercial software ABAQUS, and all the RVEs are meshed by ten node tetrahedral elements, referred to as C3D10 in ABAQUS terminology.

Table 1: Microstructural characteristics of investigated dual-phase steels. Listed data are taken from Lai et al. (2016).

Steel	V_m (%)	d_f (μm)	d_m (μm)
DP1	15	6.5	1.2
DP2	19	5.9	1.5
DP3	28	5.5	2.1
DP4	37	4.2	2.4

2.2. Constitutive behaviour of different phases

For the first numerical approach, rate-independent von Mises elastoplastic theory with isotropic hardening is assigned for both the ferrite and martensite grains. The following phenomenological flow equations are used:

$$\sigma_{y,f} = \sigma_{y0,f} + \frac{\theta_f}{\beta}(1 - exp(-\beta\varepsilon_P)) \quad for \quad \sigma_{y,f} < \sigma_y^{tr} \tag{1}$$

$$\sigma_{y,f} = \sigma_y^{tr} + \theta_{IV}(\varepsilon_P - \varepsilon_P^{tr}) \quad for \quad \sigma_{y,f} > \sigma_y^{tr} \tag{2}$$

$$\begin{aligned} \sigma_y^{tr} &= \sigma_{y0,f} + \frac{\theta_f - \theta_{IV}}{\beta} \\ \varepsilon_P^{tr} &= \frac{1}{\beta} ln\left(\frac{\theta_f}{\theta_{IV}}\right) \end{aligned} \tag{3}$$

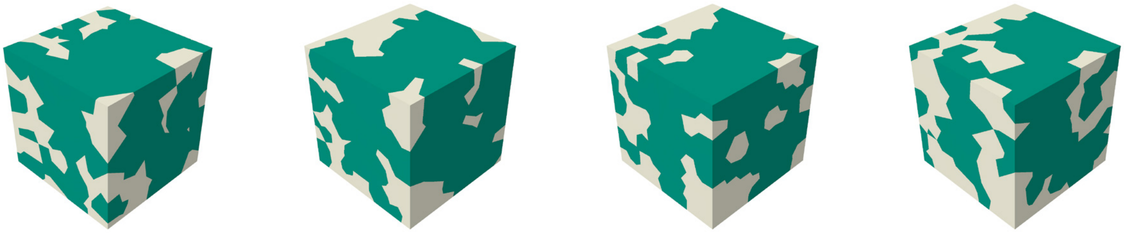

(a) (b) (c) (d)

Fig. 1: Artificially generated dual-phase steel microstructures that belong to DP1 (a), DP2 (b), DP3 (c), and DP4 (d).

The parameters for the ferrite phase are taken from Lai et al. (2016) and presented below in Table 2, where $\sigma_{y,f}$ is the current yield stress, $\sigma_{y0,f}$ is the initial yield stress, α_f and β are parameters that are related to the average ferrite grain size. θ_f is the initial, θ_{IV} is the stage-IV hardening rate and it is taken to be 100 MPa for all the steels investigated in this study. Finally, σ_y^{tr} and ε_P^{tr} respectively represent the flow stress and the plastic strain.

Table 2: Parameter set used for ferrite flow curves(Lai et al. (2016)).

Steel	$\sigma_{y0,f}$ *(MPa)*	α_f *(GPa)*	β *(GPa)*	θ_f *(MPa)*
DP1	250	4.9	11	4895
DP2	279	6	13	5980
DP3	300	8.9	17	8925
DP4	307	10.3	20	10260

The flow behavior of the martensitic phase is governed by the phenomenological equations and parameter sets given by Pierman et al. (2014):

$$\sigma_{y,m} = \sigma_{y0,m} + k_m(1 - exp(-\varepsilon_P n_m)) \tag{4}$$

where $\sigma_{y,m}$ is the current yield stress, ε_P is the accumulated plastic strain, and $\sigma_{y0,m}$, k_m, n_m are material parameters. C_m is the martensite carbon content in wt%, whose effect on strain hardening is given below

$$\sigma_{y0,m} = 300 + 1000C_m^{1/3}. \tag{5}$$

The hardening modulus k_m reads

$$k_m = \frac{1}{n_m}\left[a + \frac{bC_m}{1 + \left(\frac{C_m}{C_0}\right)^q}\right] \tag{6}$$

with a=33 GPa, b=36 GPa, C_0=0.7, q=1.45, n_m=120, C_m=0.3 wt%.

For the second numerical approach, the crystal plasticity constitutive model is assigned to ferrite phase (see Huang (1991)) while martensite is still governed by the J2 plasticity with isotropic hardening. The plastic slip rate in each slip system, $\dot{\gamma}^{(\alpha)}$, is obtained through a classical power law relation,

$$\dot{\gamma}^{(\alpha)} = \dot{\gamma}_0\left|\frac{\tau^{(\alpha)}}{g^{(\alpha)}}\right|^{1/m} \mathrm{sign}(\tau^{(\alpha)}) \tag{7}$$

where, $\tau^{(\alpha)}$ is the resolved Schmid stress on the slip systems, $\dot{\gamma}_0$ is the initial slip rate, and $g^{(\alpha)}$ is the slip resistance on each slip system, which governs the hardening of the material and evolves according to

$$\dot{g}^{(\alpha)} = \sum_{\beta=1}^{n} h^{\alpha\beta}\left|\dot{\gamma}^{\beta}\right| \tag{8}$$

where $h^{\alpha\beta}$ is the latent hardening matrix. This matrix measures the strain hardening due to shearing of slip system β on slip system α and it is defined as

$$h^{\alpha\beta} = q^{\alpha\beta} h^{(\beta)} \tag{9}$$

where $q^{\alpha\beta}$ is the latent hardening matrix and $h^{(\beta)}$ represents the self-hardening rate, for which a simple form is used (see e.g. (Peirce et al., 1982))

$$h^{\alpha\alpha} = h_0 \mathrm{sech}^2 \left| \frac{h_0 \gamma}{g_s - g_0} \right| \tag{10}$$

with h_0, g_0, g_s are initial hardening rate, the initial slip resistance and saturation value of the slip resistance, respectively. The exponent a is considered as a constant material parameter. The above presented relations summarizes the main equations for the calculation of plastic slip in each slip system in single crystal plasticity framework. After obtaining the plastic slip value in each slip system, the plastic strain and the stress should be calculated. For more details on the plastic strain decomposition, the incremental calculation of plastic strain and stress the readers are referred to the literature (see e.g. Huang (1991), Yalcinkaya et al. (2008)). The model is employed here for the simulation of plastic behavior polycrystal aggregates, where the grain structure is obtained through Voronoi tesselation using Neper software. In each grain with different orientation the crystal plasticity model runs resulting in a heterogeneous stress and strain distribution.

2.3. Boundary conditions

It is well established that the stress triaxiality (T), which is defined as

$$\begin{aligned} T &= \tfrac{\Sigma_h}{\Sigma_{eq}} \\ \Sigma_h &= \tfrac{\Sigma_{11}+\Sigma_{22}+\Sigma_{33}}{3} \\ \Sigma_{eq} &= \tfrac{1}{\sqrt{2}} \sqrt{(\Sigma_{11}-\Sigma_{22})^2 + (\Sigma_{11}-\Sigma_{33})^2 + (\Sigma_{33}-\Sigma_{22})^2} \end{aligned} \tag{11}$$

with Σ_h and Σ_{eq} being respectively the hydrostatic and equivalent von Mises stresses, has a pronounced effect on damage, localization and fracture. In the FE calculations performed here, axisymmetric tension is imposed on the RVEs, while keeping the stress triaxiality constant throughout the entire loading. $T = 1/3$ corresponds to uniaxial tensile loading. For $T > 1/3$, the RVE represents a material point in the center of the minimum cross-section of a notched tensile sample, where the stress triaxiality remains more or less constant during deformation (see e.g Tekoğlu and Pardoen (2010) and references therein).

In order to enforce periodicity, all the faces of an RVE are kept straight during the entire loading. For this purpose, first, three arbitrary nodes, M_1, M_2, and M_3 are selected respectively on the right, top, and front surfaces of the RVE; see Fig. 2. Then u_i ($i \in \{1, 2, 3\}$) displacements of all the other nodes on the surface which contains node M_i are coupled to the u_i displacement of node M_i. Similarly, u_i displacements of all the nodes on the surface opposite to the one which contains node M_i are coupled to the negative value of the u_i displacement of node M_i. These couplings are achieved by the following linear equations

$$\begin{aligned} u_1(L_1, x_2, x_3) &- u_1^M = 0, \\ u_1(0, x_2, x_3) &+ u_1^M = 0, \\ u_3(x_1, x_2, L_3) &- u_3^M = 0, \\ u_3(x_1, x_2, 0) &+ u_3^M = 0, \\ u_2(x_1, L_2, x_3) &- u_2^M = 0, \\ u_2(x_1, 0, x_3) & = 0. \end{aligned} \tag{12}$$

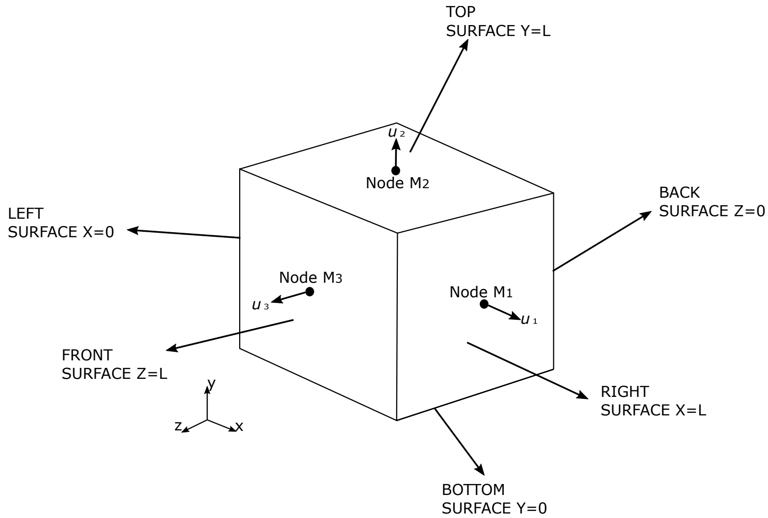

Fig. 2: A unit cell showing nodes M_1, M_2, M_3 and surface names. Node M_1 is on right, M_2 is on top, M_3 is on front surface. Displacement u_1 of node M_1, u_2 of node M_2 and u_3 of node M_3 are coupled to selected surfaces.

The stress ratios that need to be imposed on the RVE to keep T constant reads

$$\Sigma_{11} = \Sigma_{33} = \frac{3T - 1}{3T + 2}\Sigma_{22}, \tag{13}$$

where the predominant loading is taken to be applied in the x_2 direction. For the nodes on the bottom surface of the RVE, u_2 displacements are fixed while imposing zero tractions in the x_1 and x_3 directions. On the reaming surfaces of the RVE, uniformly distributed loads acting in the surface normal directions are imposed, again letting the tractions in the directions perpendicular to the surface normals to be zero. As a result, the top surface of the RVE is subjected to Σ_{22}, left and right surfaces to Σ_{11}, and front and back surfaces to Σ_{33}; see Fig. 2. The stress ratios are kept constant and equal those given in Eq. (13) by using the Riks algorithm provided by ABAQUS (see Simulia (2010)).

The method to keep the stress triaxality constant described above works perfectly fine for the calculations performed in this paper, where there is no softening. For a more general method to perform RVE calculations under constant stress triaxiality, the reader is referred to Tekoğlu (2014).

2.4. Overall response of the RVEs

In order to determine the overall response of the RVEs, the fundamental theorem of homogenization

$$\Sigma_{ij} = \frac{1}{V}\int_V \sigma_{ij} dV \tag{14}$$

is employed, which relates mesoscopic stress tensor components Σ_{ij} ($i, j \in \{1, 2, 3\}$) for an RVE with a volume V, to the local Cauchy stress components σ_{ij} in the RVE. Accordingly, Σ_{ij} for an RVE reads

$$\Sigma_{ij} = \frac{\sum_{m=1}^{N}(\sum_{q=1}^{p} \sigma_{ij}^{\{q\}} v^{\{q\}})^{\{m\}}}{V} \tag{15}$$

where N is the number of elements, p is the total number of integration points ($p = 4$ for C3D10 elements), and v is the local volume value at the corresponding integration point. The total volume V of the RVE, which remains as a rectangular prism in the entire course of the deformation, is calculated by simply multiplying the current edge lengths of the RVE: $V = L_1 \times L_2 \times L_3$. The mesoscopic principal strain components for the RVE, E_{ii}, are given by

$$E_{ii} = ln\left(\frac{L_i}{L_{i0}}\right), \tag{16}$$

with L_{i0} being the initial edge lengths of the RVE. The equivalent von Mises strain can then be calculated by using

$$E_{eq} = \frac{2}{3\sqrt{2}} \sqrt{(E_{11} - E_{22})^2 + (E_{11} - E_{33})^2 + (E_{33} - E_{22})^2} \tag{17}$$

3. Results and discussion

It this section the numerical results, obtained from the RVE calculations, are presented for axisymmetric tensile loading with stress triaxiality values of $T = 1/3$, and $T > 1/3$.

3.1. Uniaxial tensile loading ($T = 1/3$)

Initially, the J2 plasticity with isotropic hardening is assigned to both phases in the RVE, where the individual flow behavior of ferrite and martensite phases are governed by the relations presented in (1)-(3) and (4)-(6) respectively. The resulting flow curves are illustrated in Fig. 3. The variations observed in the ferrite flow response are due to the ferrite grain size. While the Hall-Petch effect dominates the plasticity behavior of ferrite, the martensite phase response is independent of the grain size. On the other hand, the constitutive response of martensite is influenced substantially by its carbon content. Although in all of the investigated cases, the martensite carbon content (C_m) is 0.3 wt%, the flow curves with 0.1, 0.2 and 0.4 wt% are presented in Fig. 3(b) nevertheless, to illustrate the effect of varying C_m.

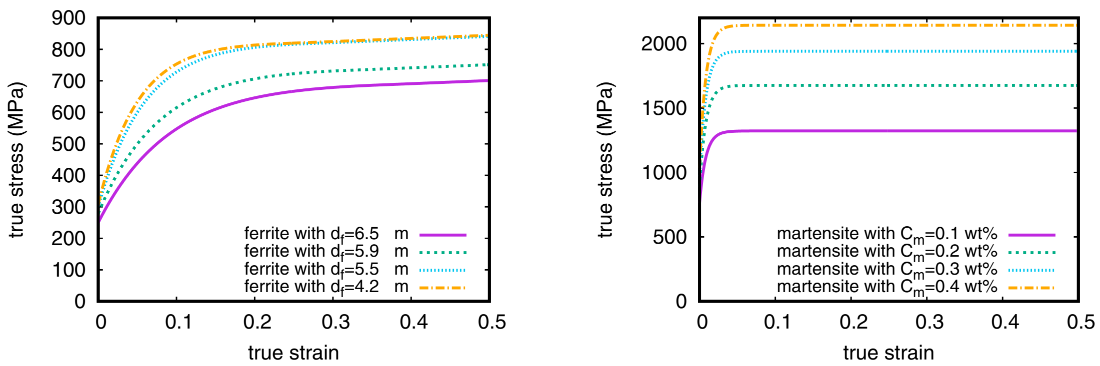

(a) (b)

Fig. 3: Flow curves of (a) ferrite and (b) martensite phases.

Next, the RVE simulations are conducted for the dual phase material with the above presented individual flow curves, where the modulus of elasticity and Poisson's ratio are taken as E=210 GPa and ν=0.3 for both phases. The resulting equivalent stress-strain curves are compared with experimental results from Lai et al. (2016) in Fig 4. The J2 based plasticity simulation results show good agreement with experimental ones, which gives the confidence for the generated RVE to be used in the following simulations. The results show that, as expected the yield and the ultimate tensile strengths increase with increasing martensite volume fractions.

Figure 5 shows the deformed contour plots of equivalent stress and logarithmic principal strain in the RVEs at the equivalent strain value of E_{eq}=0.12, which is the onset of necking state for DP4 steel. Heterogeneous stress evolution is observed in all microstructures, where the stress value increases overall with increasing martensite volume fraction. Plastic deformation is obtained in all cases in the ferrite phase. Stress concentrations are observed at the sharp edges and two sharp ends of martensite islands as well as at thin martensite-martensite and ferrite-martensite grain boundaries, similar to the studies in the literature (see e.g. Kadkhodapour et al. (2011b); Ramazani et al. (2016); Hosseini-Toudeshky et al. (2015); Lai et al. (2015)). These locations are naturally more prone to damage and fracture initiation. At the same strain level, the highest stress values are obtained in the DP4 which would have the lowest

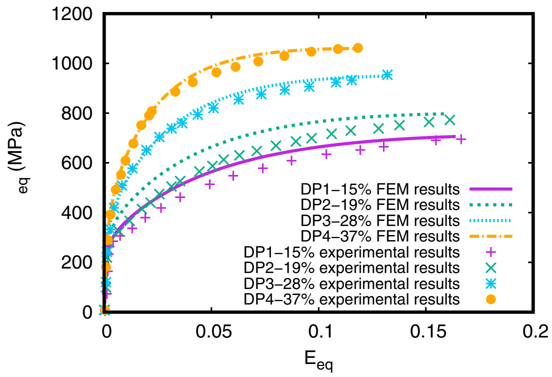

Fig. 4: Comparison of J2 plasticity based RVE calculations with the experimental data up to necking.

ductility and highest strain hardening (see e.g. Uthaisangsuk et al. (2011) for similar observations). The strain contour plots show rather large bands throughout the ferrite phase, which contradicts with the 2D RVE studies in the literature, that mention the occurrence of narrow bands (see e.g. Paul (2012); Al-Rub et al. (2015)). On the other hand, similar results are reported in the studies focussing on 3D RVEs (see e.g. Amirmaleki et al. (2016)). Strain localization occurs in ferrite region located between the two sharp ends of martensite and sharp ends of martensite as discussed in Kadkhodapour et al. (2011b). Very small strain values are obtained in martensite particles of DP1, DP2 microstructures. Some thin martensite-martensite interfaces in DP3, DP4 microstructures show high strain values. Such deformation patterns is usually seen in high martensite volume fractions(Vm>32%) according to the in situ scanning electron microscopy tests conducted by Ghadbeigi et al. (2013).

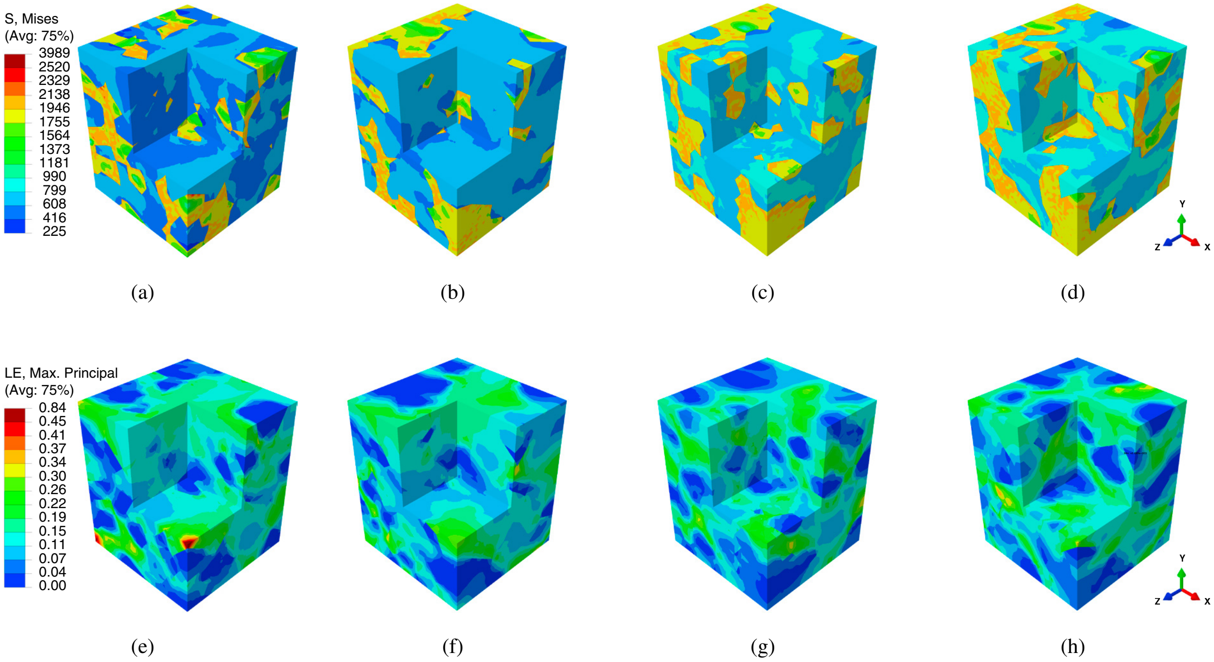

Fig. 5: Stress (a-d) and strain (e-h) contours (J2 theory) for DP1 (a,e), DP2 (b,f) ,DP3 (c,g) and DP4 (d,h) at E_{eq} = 0.12.

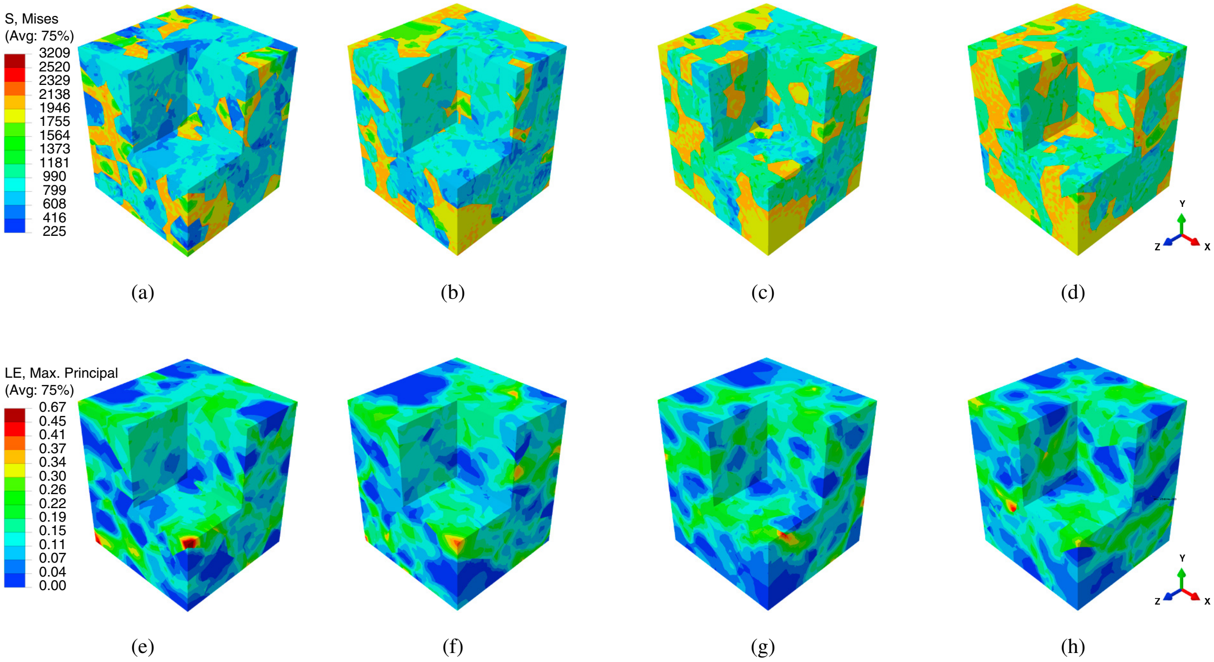

Fig. 6: Stress (a-d) and strain (e-h) contours (CPFEM) for DP1 (a,e), DP2 (b,f), DP3 (c,g) and DP4 (d,h) at E_{eq} = 0.12.

Although the J2 plasticity model is able to capture the overall stress-strain response accurately (see Fig 4), it is not able to show the relation between microstructural characteristics and stress evolution. In order to realize this, crystal plasticity constitutive model is employed to simulate the micro plasticity behavior of ferrite phase, while martensite is still modelled with J2 plasticity theory. {1 1 2} slip family is incorporated for crystal plasticity simulations of ferrite phase (see e.g. Yalcinkaya et al. (2008) and Yalcinkaya et al. (2009) for details on BCC crystal plasticity). The crystal plasticity parameters are identified through a 200 grain ferrite RVE and presented in Table 3 and the elastic constants are taken from Woo et al. (2012) as C_{11}=231.4 GPa, C_{22}=134.7 GPa and C_{44}=116.4 GPa. Initially the ferrite crystal

Table 3: Calibrated crystal plasticity parameters for ferrite.

Steel	g_s (MPa)	g_0 (GPa)	h_0 (MPa)
DP1	252	98	475
DP2	275	109	555
DP3	306.6	118.5	802.8
DP4	305	121.5	880

plasticity material parameters are identified with respect to ferrite data from DP1 which has 6.5μm average grain size (see Lai et al. (2016) for experimental data). This parameter set is used to model the behavior of DP2, DP3 and DP4 as well, which have higher volume fraction of martensite and larger ferrite grain size compared to DP1. The obtained stress-strain responses are not in agreement with the experimental data as shown in Fig. 7(a), which shows that the ferrite grain size effect on the plasticity behavior should be taken into account as well. Therefore, the crystal plasticity parameters for the ferrite phase are identified for each DP microstructure with different grain size as presented in Table 1. Then, the simulations are conducted again with these new material parameter sets, and the macroscopic results are illustrated in Fig. 7(b), which are naturally better, yet slightly overestimates the J2 ones in Fig. 4(a). Since the current crystal plasticity framework is not size dependent the parameters have to be identified accordingly for each simulation with different microstrcuture. However the usage of a strain gradient crystal plasticity framework (see e.g. Yalcinkaya et al. (2012); Yalçinkaya (2017)) would give better results with one material parameter set due to its size dependent nature.

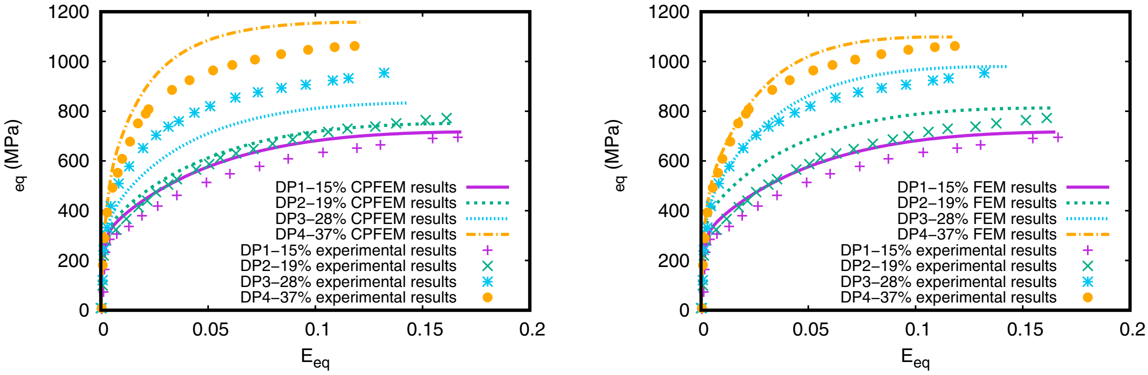

(a) (b)

Fig. 7: Uniaxial tension CPFEM simulations (a) using DP1 plasticity parameters, (b) using grain size dependent parameter set for each DP

The spatial distribution of equivalent von Mises stress and principal logarithmic strain are presented in Fig. 6. Compared to the results obtained from J2 theory (Fig. 5), strain distribution show a similar behavior, while considerable differences exist for the stress evolution in terms of both amount and heterogeneity. The most striking observation is that the crystal plasticity simulations result in higher stress values, which could be due to the stress increase at the grain boundaries because of the orientation mismatch, which does not exist in isotropic J2 simulations. Moreover, CPFEM gives more heterogeneous stress distribution in ferrite which affects the state in martensite as well. All in all, more pronounced localizations and stress concentrations are obtained at the sharp ends of martensite through crystal plasticity calculations as in the study of Kadkhodapour et al. (2011b). Although similar strain contours are obtained, additional localized regions occur nearby martensite due to random crystallographic orientations of ferrite grains (see e.g. Woo et al. (2012)).

3.2. Axisymmetric tensile loading with higher triaxiality ($T > 1/3$)

The effect of stress triaxiality on the ductile fracture strain of metals is crucial and has been the main focus of the ductile fracture studies in the recent years (see e.g. Benzerga and Leblond (2010) for an overview). As the triaxiality increases, the total volume of voids in the specimen increases, which results in lower fracture strain. In here, the overall stress triaxiality is kept constant in RVE simulations in order to analyze its effect on void formation. For that reason, a relatively wide range of stress triaxiality values are investigated, with $T \in \{1/3, 1/2, 1, 3/2, 3\}$. The macroscopic results show that the value of stress triaxiality does not affect the overall equivalent stress-strain response, since the constitutive behavior is independent of varying triaxiality. On the other hand, the effect is clearly visible in microstructure evolution at RVE level. The pressure and logarithmic strain contour plots of DP4 steel is investigated at E_{eq}=0.1 in Fig. 8. High negative internal pressure means high positive hydrostatic stress, that result in high local T and possible void formation (see Kadkhodapour et al. (2011a)). High negative pressure locations are observed initially at ferrite-martensite grain boundaries at low T values. They happen to occur also at ferrite-ferrite boundaries as triaxiality increases. Apparent strain localization occur at sharp martensite ends and between two sharp ends of martensite grains with high triaxiality values due to the plastic instability between soft ferrite and elastic martensite phase. The plastic deformation in ferrite phase is constrained by martensite islands located nearby, which act as local barriers constraining deformation of ferrite, inevitably causing high triaxiality at the grain boundaries (see e.g Paul (2013); Ayatollahi et al. (2016) for the effect of triaxiality in DP steels).

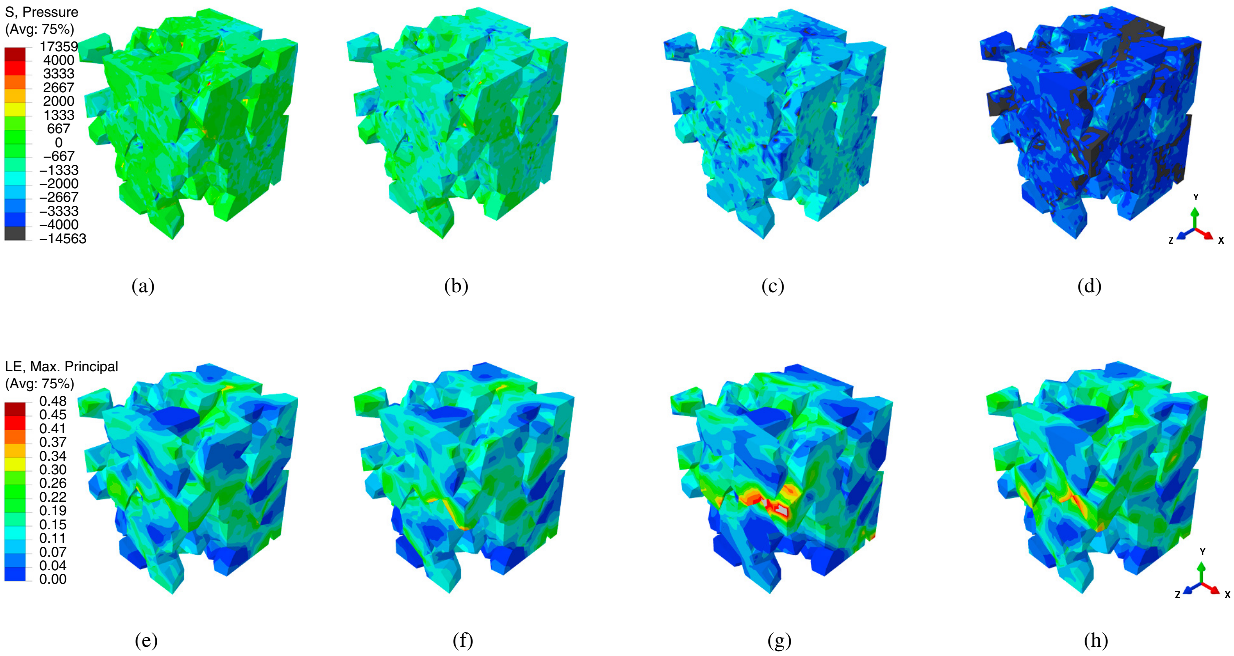

Fig. 8: Pressure (a-d) and logarithmic strain (e-h) distributions of DP4 at E_{eq}=0.1 obtained for triaxiality values 0.5 (a,e), 1 (b,f), 1.5(c,g) and 3 (d,h).

4. Conclusions

Different DP steels are investigated at RVE level through both crystal plasticity and J2 plasticity theories. The RVEs are subjected to axisymmetric tensile loadings while keeping the value of stress triaxiality constant. The main conclusions are as follows,

- Although elastoplastic and crystal plasticity simulations both give a satisfactory and similar overall behaviour, the latter method is able to capture stress partitioning and strain localizations better. Moreover crystal plasticity simulations result in higher local stresses due to orientation mismtach at the ferrite GBs which does not occur in elastoplastic calculations.
- Regardless of the constitutive model, ductility decreases with increasing martensite volume fraction. DP steels with a high V_m value have higher strengths at the expense of ductility.
- The density of void nucleation regions increase with increasing T. High local T values are observed at sharp martensite ends, and at ferrite-ferrite grain boundaries which are in the neighbourhood of martensite islands.
- Ferrite goes into plastic regime earlier than martensite. Martensite islands block the plastic deformation in ferrite, and therefore cause high T values at grain boundaries.

References

Al-Rub, R.K.A., Ettehad, M., Palazotto, A.N., 2015. Microstructural modeling of dual phase steel using a higher-order gradient plasticitydamage model. International Journal of Solids and Structures 58, 178 – 189. doi:https://doi.org/10.1016/j.ijsolstr.2014.12.029.

Amirmaleki, M., Samei, J., Green, D.E., van Riemsdijk, I., Stewart, L., 2016. 3d micromechanical modeling of dual phase steels using the representative volume element method. Mechanics of Materials 101, 27–39. doi:10.1016/j.mechmat.2016.07.011.

Avramovic-Cingara, G., Ososkov, Y., Jain, M., Wilkinson, D., 2009. Effect of martensite distribution on damage behaviour in dp600 dual phase steels. Materials Science and Engineering: A 516, 7 – 16. doi:https://doi.org/10.1016/j.msea.2009.03.055.

Ayatollahi, M.R., Darabi, A.C., Chamani, H.R., Kadkhodapour, J., 2016. 3d micromechanical modeling of failure and damage evolution in dual phase steel based on a real 2d microstructure. Acta Mechanica Solida Sinica 29, 95–110. doi:10.1016/S0894-9166(16)60009-5.

Bag, A., Ray, K.K., Dwarakadasa, E.S., 1999. Influence of martensite content and morphology on tensile and impact properties of high-martensite dual-phase steels. Metallurgical and Materials Transactions A 30, 1193–1202. doi:10.1007/s11661-999-0269-4.

Benzerga, A.A., Leblond, J.B., 2010. Ductile fracture by void growth to coalescence, volume 44 of *Advances in Applied Mechanics*, pp. 169 – 305. doi:https://doi.org/10.1016/S0065-2156(10)44003-X.

Bong, H.J., Lim, H., Lee, M.G., Fullwood, D.T., Homer, E.R., Wagoner, R.H., 2017. An rve procedure for micromechanical prediction of mechanical behavior of dual-phase steel. Materials Science and Engineering: A 695, 101 – 111. doi:https://doi.org/10.1016/j.msea.2017.04.032.

Choi, S.H., Kim, E.Y., Woo, W., Han, S., Kwak, J., 2013. The effect of crystallographic orientation on the micromechanical deformation and failure behaviors of dp980 steel during uniaxial tension. International Journal of Plasticity 45, 85 – 102. doi:https://doi.org/10.1016/j.ijplas.2012.11.013.

Ghadbeigi, H., Pinna, C., Celotto, S., 2013. Failure mechanisms in dp600 steel: Initiation, evolution and fracture. Materials Science and Engineering A 588, 420–431. doi:10.1016/j.msea.2013.09.048.

Hosseini-Toudeshky, H., Anbarlooie, B., Kadkhodapour, J., 2015. Micromechanics stress-strain behavior prediction of dual phase steel considering plasticity and grain boundaries debonding. Materials and Design 68, 167 – 176. doi:10.1016/j.matdes.2014.12.013.

Huang, Y., 1991. A user-material subroutine incorporating single crystal plasticity in the abaqus finite element program. Mech. Report 178. Division of Applied Sciences, Harvard University, Cambridge, MA .

Jafari, M., Ziaei-Rad, S., Saeidi, N., Jamshidian, M., 2016. Micromechanical analysis of martensite distribution on strain localization in dual phase steels by scanning electron microscopy and crystal plasticity simulation. Materials Science and Engineering: A 670, 57 – 67. doi:https://doi.org/10.1016/j.msea.2016.05.094.

Kadkhodapour, J., Butz, A., Ziaei Rad, S., 2011a. Mechanisms of void formation during tensile testing in a commercial, dual-phase steel. Acta Materialia 59, 2575–2588. doi:10.1016/j.actamat.2010.12.039.

Kadkhodapour, J., Butz, A., Ziaei-Rad, S., Schmauder, S., 2011b. A micro mechanical study on failure initiation of dual phase steels under tension using single crystal plasticity model. International Journal of Plasticity 27, 1103 – 1125. doi:https://doi.org/10.1016/j.ijplas.2010.12.001.

Kadkhodapour, J., Schmauder, S., Raabe, D., Ziaei-Rad, S., Weber, U., Calcagnotto, M., 2011c. Experimental and numerical study on geometrically necessary dislocations and non-homogeneous mechanical properties of the ferrite phase in dual phase steels. Acta Materialia 59, 4387 – 4394. doi:https://doi.org/10.1016/j.actamat.2011.03.062.

Kang, J., Ososkov, Y., Embury, J.D., Wilkinson, D.S., 2007. Digital image correlation studies for microscopic strain distribution and damage in dual phase steels. Scripta Materialia 56, 999 – 1002. doi:https://doi.org/10.1016/j.scriptamat.2007.01.031.

Kim, J.H., Kim, D., Barlat, F., Lee, M.G., 2012. Crystal plasticity approach for predicting the bauschinger effect in dual-phase steels. Materials Science and Engineering: A 539, 259 – 270. doi:https://doi.org/10.1016/j.msea.2012.01.092.

Lai, Q., Bouaziz, O., Gouné, M., Brassart, L., Verdier, M., Parry, G., Perlade, A., Bréchet, Y., Pardoen, T., 2015. Damage and fracture of dual-phase steels : Influence of martensite volume fraction. Materials Science and Engineering A 646, 322–331. doi:10.1016/j.msea.2015.08.073.

Lai, Q., Brassart, L., Bouaziz, O., Goune, M., Verdier, M., Parry, G., Perlade, A., Brechet, Y., Pardoen, T., 2016. Influence of martensite volume fraction and hardness on the plastic behavior of dual-phase steels: Experiments and micromechanical modeling. International Journal of Plasticity 80, 187 – 203. doi:https://doi.org/10.1016/j.ijplas.2015.09.006.

Paul, S.K., 2012. Micromechanics based modeling of dual phase steels: Prediction of ductility and failure modes. Computational Materials Science 56, 34–42. doi:10.1016/j.commatsci.2011.12.031.

Paul, S.K., 2013. Effect of martensite volume fraction on stress triaxiality and deformation behavior of dual phase steel. Materials and Design 50, 782–789. doi:10.1016/j.matdes.2013.03.096.

Peirce, D., Asaro, R., Needleman, A., 1982. An analysis of nonuniform and localized deformation in ductile single crystals. Acta metallurgica 30, 1087–1119. doi:https://doi.org/10.1016/0001-6160(82)90005-0.

Pierman, A.P., Bouaziz, O., Pardoen, T., Jacques, P., Brassart, L., 2014. The influence of microstructure and composition on the plastic behaviour of dual-phase steels. Acta Materialia 73, 298 – 311. doi:https://doi.org/10.1016/j.actamat.2014.04.015.

Quey, R., Dawson, P., Barbe, F., 2011. Large-scale 3d random polycrystals for the finite element method: Generation, meshing and remeshing. Computer Methods in Applied Mechanics and Engineering 200, 1729 – 1745. doi:https://doi.org/10.1016/j.cma.2011.01.002.

Ramazani, A., Abbasi, M., Kazemiabnavi, S., Schmauder, S., Larson, R., Prahl, U., 2016. Development and application of a microstructure-based approach to characterize and model failure initiation in dp steels using xfem. Materials Science and Engineering A 660, 181–194. doi:10.1016/j.msea.2016.02.090.

Simulia, D., 2010. Abaqus/standard theory manual, version 6.14. Dassault Systemes Simulia Corporation, Providence, RI .

Tasan, C., Diehl, M., Yan, D., Bechtold, M., Roters, F., Schemmann, L., Zheng, C., Peranio, N., Ponge, D., Koyama, M., Tsuzaki, K., Raabe, D., 2015. An overview of dual-phase steels: Advances in microstructure-oriented processing and micromechanically guided design. Annual Review of Materials Research 45, 391–431. doi:10.1146/annurev-matsci-070214-021103.

Tekoğlu, C., 2014. Representative volume element calculations under constant stress triaxiality, lode parameter, and shear ratio. International Journal of Solids and Structures 51, 4544 – 4553. doi:https://doi.org/10.1016/j.ijsolstr.2014.09.001.

Tekoğlu, C., Pardoen, T., 2010. A micromechanics based damage model for composite materials. International Journal of Plasticity 26, 549 – 569. doi:https://doi.org/10.1016/j.ijplas.2009.09.002.

Uthaisangsuk, V., Prahl, U., Bleck, W., 2011. Modelling of damage and failure in multiphase high strength dp and trip steels. Engineering Fracture Mechanics 78, 469 – 486. doi:https://doi.org/10.1016/j.engfracmech.2010.08.017.

Woo, W., Em, V., Kim, E.Y., Han, S., Han, Y., Choi, S.H., 2012. Stress–strain relationship between ferrite and martensite in a dual-phase steel studied by in situ neutron diffraction and crystal plasticity theories. Acta Materialia 60, 6972 – 6981. doi:https://doi.org/10.1016/j.actamat.2012.08.054.

Yalçinkaya, T., 2017. Strain Gradient Crystal Plasticity: Thermodynamics and Implementation. Springer International Publishing, Cham. pp. 1–32. doi:10.1007/978-3-319-22977-5_2-1.

Yalcinkaya, T., Brekelmans, W., Geers, M., 2012. Non-convex rate dependent strain gradient crystal plasticity and deformation patterning. International Journal of Solids and Structures 49, 2625 – 2636. doi:https://doi.org/10.1016/j.ijsolstr.2012.05.029.

Yalcinkaya, T., Brekelmans, W.A.M., Geers, M.G.D., 2008. BCC single crystal plasticity modeling and its experimental identification. Modelling and Simulation in Materials Science and Engineering 16, 085007. doi:10.1088/0965-0393/16/8/085007.

Yalcinkaya, T., Brekelmans, W.A.M., Geers, M.G.D., 2009. A composite dislocation cell model to describe strain path change effects in BCC metals. Modelling and Simulation in Materials Science and Engineering 17, 064008. doi:10.1088/0965-0393/17/6/064008.